AIP Journal of Applied Physics

Electrical transport properties and magnetic cluster glass behavior of Nd0.7Sr0.3MnO3 nanoparticles

B. Roy, A. Poddar, and S. Das

Citation: J. Appl. Phys. 100, 104318 (2006); doi: 10.1063/1.2387056
View online: http://dx.doi.org/10.1063/1.2387056
View Table of Contents: http://jap.aip.org/resource/1/JAPIAU/v100/i10
Published by the AIP Publishing LLC.

Electrical transport properties and magnetic cluster glass behavior of $Nd_{0.7}Sr_{0.3}MnO_3$ nanoparticles

B. Roy,[a] A. Poddar, and S. Das[b]
ECMP Division, Saha Institute of Nuclear Physics, 1/AF Bidhannagar, Kolkata 700 064, India

(Received 5 May 2006; accepted 7 September 2006; published online 28 November 2006)

The transport and magnetic properties have been investigated in $Nd_{0.7}Sr_{0.3}MnO_3$ nanoparticles prepared by the sol-gel method. The resistivity (ρ) increases with the decrease of the particle size due to the enhancement of the grain boundary effect. $\rho(T)$ shows two distinct transitions for all the samples such as metal-insulator transition and transition due to the barrier caused by the grain boundary effect. The thermopower (S) is found to be negative and at high temperature S follows the adiabatic small polaron hopping theory. In the metallic region the spin wave contribution is found to be dominant in the temperature dependence of the thermopower. The magnetoresistance (MR) of the ultrafine particles increases with the decrease of particle size indicating substantial contribution from the grain boundaries. Spin polarized intergrain tunneling effect plays an important role in the MR of a smaller size particle, whereas in the case of samples of higher dimension spin fluctuation contributes predominantly. The field cooled (FC) and zero field cooled (ZFC) magnetizations display a paramagnetic-ferromagnetic transition at T_C with a large magnetic irreversibility. The ZFC peak temperature T_B and the irreversibility temperature (T_{irr}) are field dependent and decrease with the decrease of the particle dimension. Magnetic measurement indicates that particles are single domain with the particles of highest dimension lying in the multidomain region. A cluster glasslike behavior of the particles is revealed from the analysis of the dc and ac magnetization data. © *2006 American Institute of Physics*. [DOI: 10.1063/1.2387056]

I. INTRODUCTION

Nanocrystalline materials have attracted considerable scientific interest because of the physics[1–4] involved in them as well as the possibility of potential applications.[5–8] The presence of a large amount of grain boundaries and/or the broad distribution of interatomic spacings in the grain boundaries give rise to the unusual properties differing from the properties of the conventional polycrystals or single crystals with the same chemical composition. Magnetic nanoparticles with smaller grain sizes exhibit richer electronic and magnetic properties arising from the structural and magnetic disorders in the grain surfaces. Recently, modification of the properties of nanosized perovskites has created much interest.[9–16] The doped manganites with strongly correlated electrons exhibit fascinating properties originating from the strong interplay between charge, spin, orbital, and structural degrees of freedom.[17–20] Doped manganites $R_{1-x}A_xMnO_3$ (R=rare earth and A=divalent alkaline earth metal) undergoes a paramagnetic (PM) insulator to ferromagnetic (FM) metal transition and shows colossal magnetoresistance (CMR) phenomena in the vicinity of the transition. The observed correlation between the metallicity and ferromagnetism in manganites has been explained within the framework of the double exchange (DE) mechanism which describes the electronic hopping between neighboring Mn e_g orbitals. However, the DE mechanism cannot explain the entire observed phase diagram. In addition to DE, the polaron effect due to a very strong electron phonon coupling coming from the Jahn-Teller (JT) lattice distortion of the Mn^{3+} is very helpful to explain the resistivity and magnetoresistance of $R_{1-x}A_xMnO_3$ compounds.[21] Besides the DE interaction, the phase diagram of manganites is depicted with many other competing interactions such as antiferromagnetic superexchange, orbital ordering (OO), charge ordering (CO), etc.[18] For R=Nd, the parent compound $NdMnO_3$ is an insulating antiferromagnet. $Nd_{1-x}Sr_xMnO_3$ shows interesting phenomena different from that observed in $La_{1-x}A_xMnO_3$ due to the weakening of the DE interaction caused by the larger lattice distortion for smaller Nd ions. With partial substitution of Nd by Sr, $Nd_{1-x}Sr_xMnO_3$ becomes a canted spin ferromagnet and insulator for $0 \leqslant x \leqslant 0.1$, a ferromagnetic insulator for $0.1 \leqslant x \leqslant 0.15$, and a ferromagnetic metal for $0.2 \leqslant x \leqslant 0.48$.[22] The epitaxial thin film of $Nd_{2/3}Sr_{1/3}MnO_3$ shows the highest MR in excess of 99.999 near 60 K in a field of 8 T.[23] Most of the works on the nanoparticles of manganites are based on the resistivity and magnetoresistance, but thermopower data and magnetic information about the nanoparticles of manganites are very rare. We have chosen $Nd_{0.7}Sr_{0.3}MnO_3$ to study the modification of the transport and magnetic properties due to the size of the nanoparticles.

II. EXPERIMENT

Nanocrystalline samples of $Nd_{0.7}Sr_{0.3}MnO_3$ were prepared following a usual citrate gel process using nitrates (readily prepared) of the constituent materials. The gel was burnt to dried powder and the collected powder was heated at 400 °C for a long time giving a black powder. The final precursor was separated into parts and pressed into pellets.

[a]Present address: Ramakrishna Mission Vidyamandira, Belur Math, Howrah 711 202, India.
[b]Electronic mail: sailendranath.das@saha.ac.in

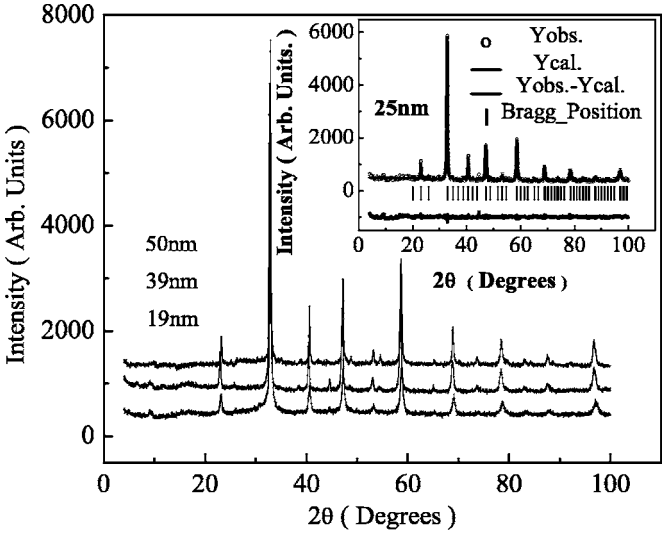

FIG. 1. Powder x-ray diffraction pattern of $Nd_{0.7}Sr_{0.3}MnO_3$ nanoparticles at room temperature. The inset shows the observed and calculated x-ray diffraction patterns (Rietveld analysis) of the 25 nm sample. The vertical marks show the position of the allowed reflections.

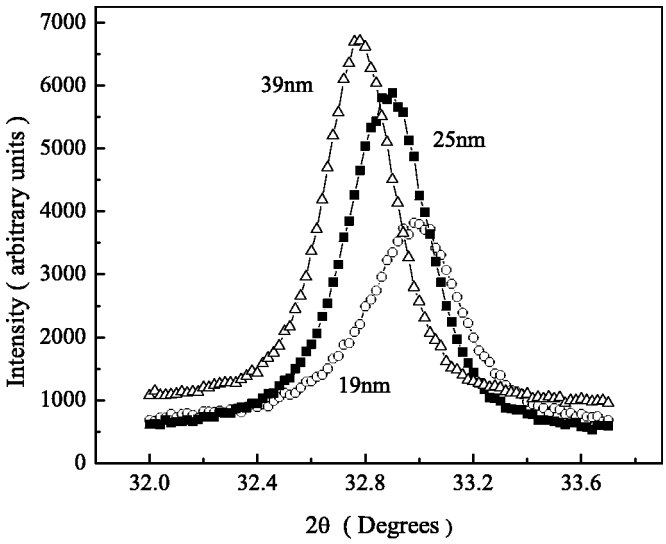

FIG. 2. X-ray diffraction profiles for the most intense peak of the $Nd_{0.7}Sr_{0.3}MnO_3$ sample with particle diameters of 19, 25, and 39 nm.

Particles with different sizes were obtained by controlling the annealing temperature (T_{ann}). In order to obtain samples of different particle sizes the pellets were annealed separately for 6 h at 800, 900, 1000, and 1100 °C under air atmosphere with subsequent slow cooling to room temperature. The phase purity of the samples was checked by x-ray powder diffraction (Phillips PW diffractometer 1820) using Cu $K\alpha$ radiation. The x-ray diffraction data of the four samples were analyzed with the Rietveld method. The size of the particle was determined from the x-ray peak width using Scherer's formula. The particle size was also measured by the transmission electron microscope (TEM).

Magnetic properties of the samples have been measured using a Quantum Design MPMS5 superconducting quantum interference device (SQUID) with magnetic fields from 10 Oe to 50 KOe. Hysteresis measurements were performed at several fixed temperatures as a function of the magnetic field. The temperature dependence of ac susceptibility was studied at different frequencies. The resistivity was measured by a standard four probe technique where as the magnetoresistance was measured with direct current perpendicular to the magnetic field direction in the temperature range of 4–300 K using an Oxford cryostat equipped with 8 T magnetic field. The thermopower measurements were performed with a homebuilt instrument in a cryostat working from 320 K down to liquid nitrogen temperature.

III. RESULTS AND DISCUSSIONS

A. XRD and TEM measurements

The x-ray powder diffraction reveals a single phase for all the samples and the diffraction patterns are broad due to the formation of fine powder. Figure 1 shows the x-ray diffraction patterns of the samples with the inset displaying the full pattern of the Rietveld analysis result for the 25 nm sample using the FULLPROF program.[24] The x-ray Rietveld analysis shows that the samples have an orthorhombic perovskite structure with a space group *Pnma*. Table I summarizes the unit cell parameters obtained by the Rietveld analysis of the diffractograms by using the FULLPROF program. The Rietveld analysis reveals that Mn–O–Mn bond angles decrease and the bond distance increases with the decrease of the particle size. In Fig. 2 we have plotted the intensity of the largest intense peak as a function of 2θ. As the sintering temperature increases the width of the peak decreases. The systematic broadening of the x-ray diffraction (XRD) lines corresponds to the decrease of the particle size. The average particle size (D) of the particles in the samples is calculated using Scherrer's formula $D=k\lambda/\beta\cos\theta$, where k is the particle shape factor (=0.89, considering the circular shape of the nanoparticles), λ is the wavelength of Cu $K\alpha$ radiation (=1.541 Å), β is the full width at half maximum of the XRD peak, and θ is the diffraction angle of the peak. The particle size measurement from Scherrer's formula shows that the particle size increases with the increase of the annealing tem-

TABLE I. Refined x-ray structural parameters of $Nd_{0.7}Sr_{0.3}MnO_3$ nanoparticles having *Pnma* space group symmetry. Numbers in the parentheses are errors of the last significant digit.

Particle size (nm)	T_{ann} (°C)	a (Å)	b (Å)	c (Å)	Mn–O–Mn (deg)	d_{Mn-O} (Å)
19	800	5.4322(2)	7.7216(1)	5.4301(4)	152.603	1.980(4)
25	900	5.4363(5)	7.7235(2)	5.4359(9)	155.141	1.973(2)
39	1000	5.4461(1)	7.7288(5)	5.4548(0)	157.410	1.972(1)
50	1100	5.4593(3)	7.7353(2)	5.4568(1)	158.100	1.970(0)

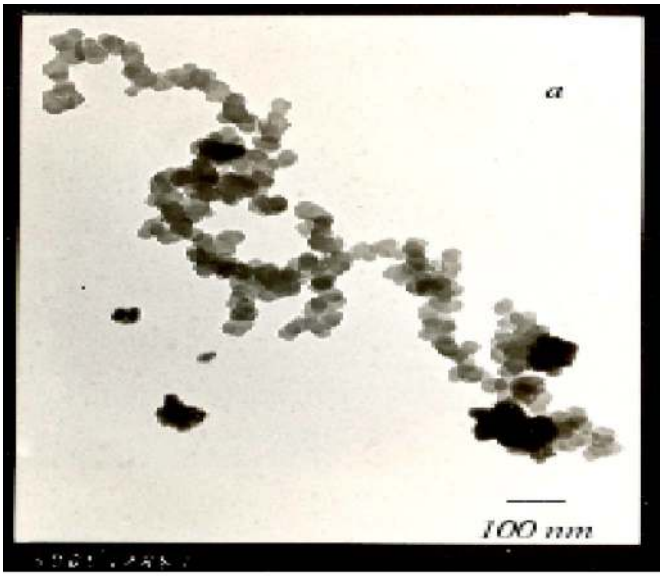

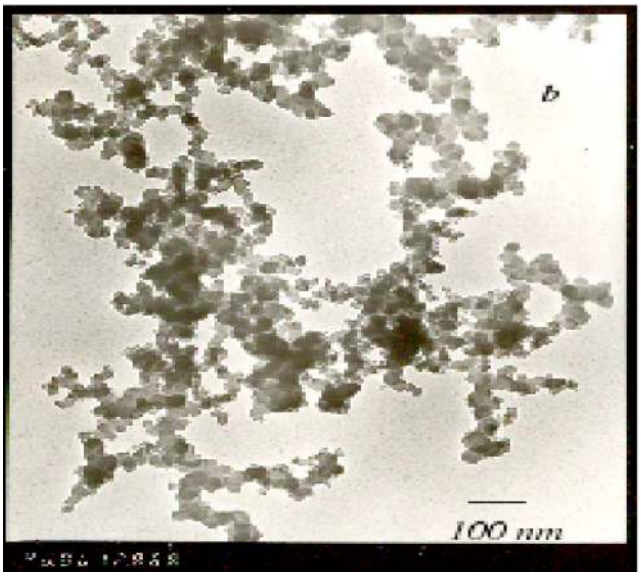

FIG. 3. Transmission electron micrograph of the $Nd_{0.7}Sr_{0.3}MnO_3$ sample with (a) 39 nm and (b) 50 nm particle sizes.

perature. The size of the particle was also confirmed by TEM measurement. The typical transmission electron microscope images of the samples (39 and 50 nm) are shown in Figs. 3(a) and 3(b). Closer inspection of the TEM images shows that the nanoparticles of the four samples studied have nearly spherelike elementary shape and the particles are arranged in chains. Analysis of the particle diameters reveals that the particle size distribution is almost narrow.

B. Resistivity

Figure 4 presents the resistivity versus temperature curves of the four samples. The zero field resistivity increases with the decrease of temperature, exhibits a pronounced peak at T_{MI} and then decreases as the temperature is further lowered below T_{MI}. At low temperature the resistivity shows a rapid rise as the temperature decreases. The compound was found to undergo a paramagnetic to ferromagnetic transition at a temperature T_C (Sec. III E). Thus the

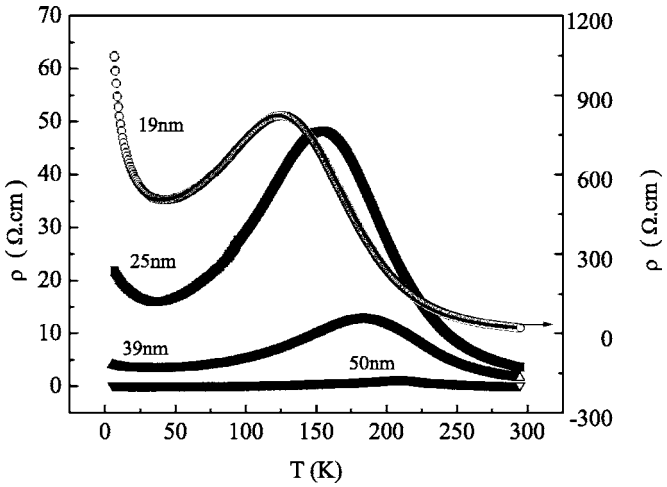

FIG. 4. Temperature dependence of resistivity of $Nd_{0.7}Sr_{0.3}MnO_3$ nanoparticles.

evolution of the negative temperature coefficient of resistivity ($d\rho/dT<0$) above T_{MI} indicates an insulating nature, whereas the positive temperature coefficient ($d\rho/dT>0$) below this temperature displays a metallic behavior of the sample thereby marking an insulator-metal transition at T_{MI} together with a paramagnetic to ferromagnetic transition in the vicinity. From the figure it is evident that the resistivity of the compound increases with the decrease of the particle size, implying that the decrease of the grain size relatively increases the insulating regions due to the enhancement of the grain boundary effect. From the Rietveld analysis of the x-ray diffraction patterns we have found reduction of bond angles and enhancement of the bond distance with the decrease of particle size. The combined effect results into a decrease in the effective bandwidths and consequent reduction of the transfer integral with the decrease of the particle size enhances the resistivity. The metal-insulator transition temperature also decreases with the reduction of the particle size. At $T<50$ K all the samples exhibit a minima in $\rho(T)$ in the metallic phase and a rapid rise in resistivity indicating an insulating nature in this region. The temperature of the minima below which the upturn of $\rho(T)$ takes place decreases with the increase of the particle size. The resistivity increases sharper as the particle size decreases. The enhancement of the resistivity of samples of the same composition but different size must be related to the dimension of the particles. The increase in the low temperature resistivity indicates an insulatinglike barrier in the nanoparticles. The insulating property exhibited by the $\rho(T)$ curve may be due to the breakdown of the DE mechanism in the disordered interfacial region caused by the broken Mn–O–Mn bonds at the surface of the grains and the translational symmetry breaking of the lattice. Nanoparticles may be considered as a core-shell-type structure,[9,12,25,26] where the core consists of a FM metallic part similar to a bulk material and the surface shell is insulating. Spin disordered surface layers and the thickness of the shell increase with the reduction of the grain size. Balcells *et al.*[9] used the theoretical expression proposed by Sheng *et al.*[27] for the hopping conductivity in granular materials and gave an experimental verification of a Coulomb

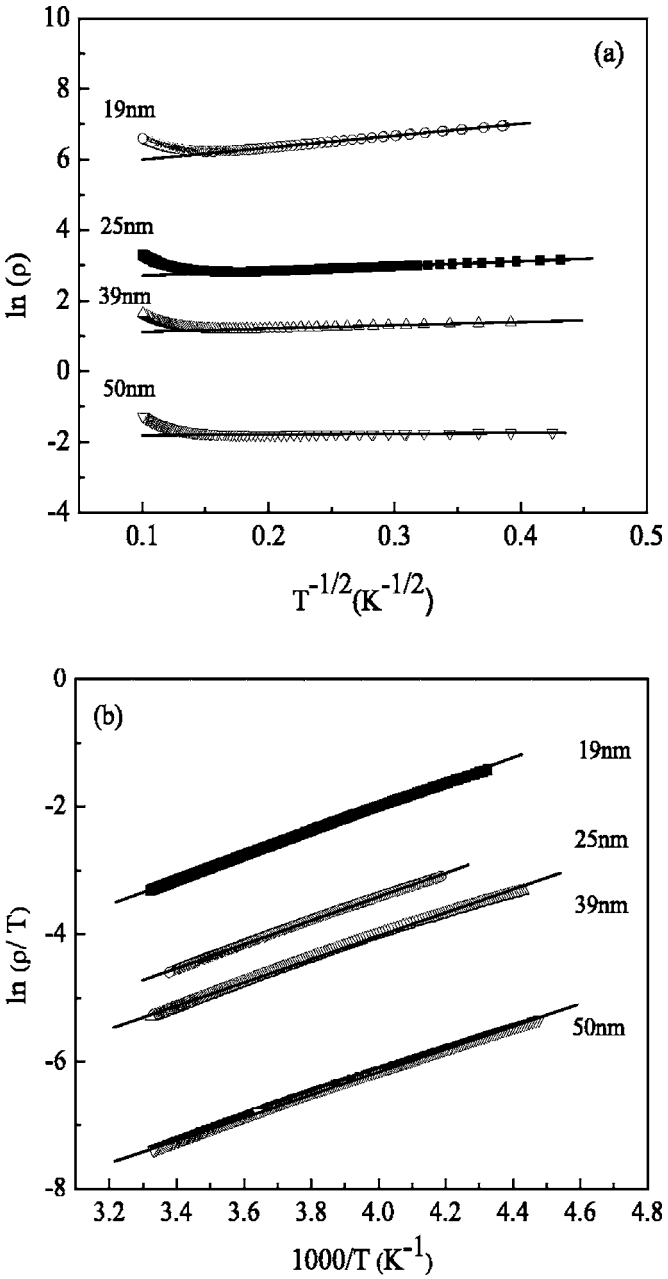

FIG. 5. (a) Plot of $\ln(\rho)$ vs $T^{-1/2}$ curves and (b) plot of $\ln(\rho/T)$ vs $1000/T$ curves.

blockade contribution to the resistivity in granular manganese perovskites. The granular metals are found to follow a relation $\rho(T) \sim \exp\sqrt{\Delta/T}$, where Δ is proportional to E_c which is the charging energy required to create a positive-negative charged pair of grains. We have plotted $\ln \rho$ vs $T^{-1/2}$ [Fig. 5(a)] and the curve shows linearity with increasing slope as the size decreases. The linear curve provides us with the values of E_c which increases with the decrease of the size. The estimated values of E_c are 11.5 K for 19 nm and 0.051 K for 50 nm. E_c is found to be proportional to $1/D$ which is expected for a Coulomb barrier of electrostatic origin associated with grain charging.[27] Therefore we can conclude that the enhancement of the resistivity at low temperatures is originated from the Coulomb barrier superposed over the tunnel barrier of magnetic and structural origins. To analyze our data in the metallic regime we have used the following expression:[28]

$$\rho(T) = \rho(0) + \rho_2 T^2 + \rho_{9/2} T^{9/2}, \tag{1}$$

where ρ_2 represents the electron-electron scattering and $\rho_{9/2}$ represents electron-magnon scattering. The data fit well with the above expression in the metallic region (not shown in the figure), suggesting that transport mechanism in this region can be attributed to the carrier-magnon scattering. In the paramagnetic region above T_{MI} the charge conduction takes place according to the theory of Emin and Holstein for adiabatic small polaron hopping,[29] which can be expressed as

$$\rho(T) = BT \exp(E_\rho / k_B T), \tag{2}$$

where B is the resistivity coefficient, E_ρ is the activation energy, and k_B is the Boltzmann constant. Austin and Mott[30] have shown that the activation energy E_ρ is given by the following relation:

$$\begin{aligned} E_\rho &= W_H + W_D/2 \quad \text{for } T > \theta_D/2 \\ &= W_D \qquad\quad \text{for } T < \theta_D/4, \end{aligned} \tag{3}$$

where W_D is the disorder energy and θ_D is the characteristic Debye temperature and the polaron hopping energy W_H is the difference of activation energies E_ρ and E_S obtained by fitting the resistivity and thermoelectric power (TEP) versus temperature curves ($W_H = E_\rho - E_S$). In Fig. 5(b) we have plotted $\ln(\rho/T)$ vs $1000/T$ and the linear behavior of the curves support the adiabatic small polaron hopping conduction of the carriers. The values of $\theta_D/2$ are estimated from the temperature where the nonlinearity appears. The nature of the hopping conduction can be confirmed from Holstein's condition that the polaron bandwidth J should satisfy the inequalities, $J > \lambda$ (for adiabatic condition) and $J < \lambda$ (for nonadiabatic condition), where

$$\lambda = (2k_B T W_H/\pi)^{1/4} (h\nu/\pi)^{1/2}. \tag{4}$$

The polaron bandwidth (J) is calculated from the model of Mott and Davis[31] as $J \approx e^3 [N(E_F)/\epsilon^3]^{1/2}$. The dielectric constant ϵ is determined from the following relation:

$$W_H = \frac{e^2}{4\epsilon}\left(\frac{1}{r_p} - \frac{1}{R}\right), \tag{5}$$

where r_p is the polaron radius. The polaron radius is calculated from the relation $r_p = (1/2)(\pi/6)^{1/3} R$. The parameters obtained are summarized in Table III. Comparing the values of J and λ the inequality $J > \lambda$ is found to be well satisfied for the nanoparticle samples upholding the validity of the adiabatic hopping conduction. Assuming the high temperature activation energy W to be close to the hopping energy W_H one can have a rough estimate of the electron phonon coupling strength $\gamma = W_p/k_B\theta_D$, where W_p is the polaron binding energy and equal to $2W_H$ in the narrow band limit. Table III includes the calculated values of γ. The estimated parameters are in consonance with those observed by other authors in manganites.[32,33] In the case of manganites many authors[34,35] use Mott's variable range hopping model[31] to explain the conduction mechanism in the temperature region

TABLE II. Various characteristic temperatures and density of states at the Fermi level obtained from the analysis of the magnetic and electrical transport data.

Sample (nm)	T_C (K)	T_B (K)	T_{irr} (K)	Θ (K)	T_{MI} (K)	$T_0 \times 10^6$ (K)	$N(E_F)$ (eV^{-1} cm^{-1})
19	182	52	160	226	127	8.17	2.42×10^{20}
25	208	104	176	230	156	3.99	4.96×10^{20}
39	216	142	206	234	182	1.87	1.05×10^{21}

$T_{MI} < T_C < \theta_D/2$, where θ_D is the Debye temperature. Mott's variable range hopping (VRH) mechanism can be described by the following relation:

$$\rho(T) = \rho(0)\exp[(T_0/T)^{1/4}]. \quad (6)$$

The characteristic Mott temperature T_0 is expressed as $T_0 = 16\alpha^3/k_B N(E_F)$, where α describes the spatial extent of the localized wave function. The density of states at the Fermi level $N(E_F)$ is determined assuming $\alpha = 2.22$ nm^{-1}.[34] The linear dependence of $\ln(\rho)$ on $T^{-1/4}$ verifies the validity of the VRH mechanism in the temperature region $T_{MI} < T < \theta_D/2$. Tables II and III contain some of the parameters obtained from the fitting of the data with the VRH model. But in reality Mott's VRH model was derived to explain the electrical conduction between localized states in a disordered system in the low temperature region below $\theta_D/2$. In case of the nanoparticles studied here Mott's VRH model fits in the low temperature but the parameters obtained are unphysical.

C. Magnetoresistance

Figure 6 illustrates the resistivity and the change of the resistivity of the 19 nm sample in response of the fields 1, 3, and 5 T along with the temperature variation of the magnetoresistance (between $H=5$ T and $H=0$ T), which is defined as

$$\mathrm{MR} = \{[\rho(H) - \rho(0)]/\rho(0)\} \times 100, \quad (7)$$

where $\rho(0)$ is the zero field resistivity and $\rho(H)$ is the resistivity at field H. The resistivity peak temperature shifts slowly towards the higher temperature with the increase of the field and MR(T) increases with decreasing temperature, passes through a broad maximum at a temperature T_{MR} slightly higher than T_{MI} for zero field. The MR(T) curve shows a wide peak in between the resistive transition peaks for the 0 and 5 T fields, remains almost flat over a wide temperature range, and then again shows an upward turn with further decrease of the temperature at low temperature. From Fig. 7 it is evident that for the 19, 25, 39, and 50 nm samples MR(T) increases with the decrease of the particle size and the width of the MR(T) peak becomes sharper with the increase of the particle size. The nature of the MR(T) curve of the 50 nm sample is quite different from those of the three smaller size samples. It shows a sharper peak at a temperature close to T_{MI} and the peak of the MR(T) curve of the 50 nm sample increases higher than that of all other samples. The origins of the magnetoresistance at low temperature and at the peak are different.[9,36] One origin of the MR is the suppression of spin disorder through the alignment of the spins in response to the applied magnetic field and the MR reaches a maxima value at the ferromagnetic transition temperature. This MR scales with the field induced magnetization m as $-\mathrm{MR} = c(m/m_s)^2$ for $m/m_s < 0$, where m_s is the saturation magnetization. The MR decreases with the decrease of temperature and for the crystal the MR vanishes as $T \to 0$. But in polycrystalline samples the contribution to MR appears due to the intergrain spin polarized tunneling across the grain boundaries with a highest value at the lowest temperature studied. With the decrease of the particle size the disorder on the surface of the ultrafine particle increases and the spin polarized tunneling contribution enhances. We have also measured the field-dependent resistivity at different fixed temperatures to get a better picture of the phenomenon. The variation of the magnetoresistance as a function of the applied field at fixed temperatures is displayed in the inset of Fig. 7 for the 39 and 50 nm samples. In the MR(T) isotherms a sharp decrease in the MR at low field (<1 T) takes place followed by a gradual change in the high fields. In the low field region, the magnetization is not saturated, whereas in the high field region the magnetic induction becomes important. Application of a small magnetic field rearranges the domain alignment along a parallel direction. Then the spin polarized tunneling between grains enhances the conductivity. The high field MR increases with the decrease of the particle size, and the low field MR decreases with the increase of temperature and as well as with the increase of the particle size.

TABLE III. Parameters estimated from the best fit of the electrical transport data using the variable range hopping and polaron hopping models.

D (nm)	Θ_D (K)	$\nu_{ph} \times 10^{-13}$ (cm^{-1})	R (Å)	r_p (Å)	E_ρ (meV)	E_s (meV)	W_H (meV)	ϵ_p	γ	J (meV)	λ (meV)
19	500	1.04	5.441	2.193	165.3	2.0	163.3	6.0	7.59	57.84	26.63
25	503	1.05	5.445	2.95	161.1	3.5	157.6	6.21	7.26	78.64	26.52
39	512	1.07	5.455	2.199	157.7	4.3	153.4	6.37	6.93	110.13	26.50
50	519	1.08	5.462	2.201	154.2	13.6	140.6	6.95	6.30	150.6	26.14

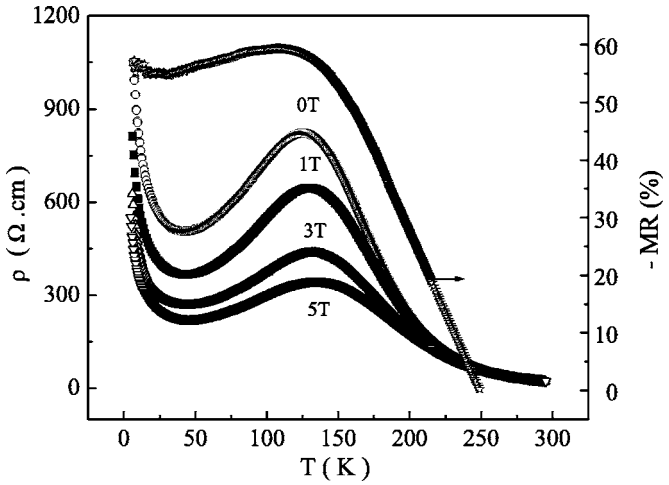

FIG. 6. Field dependent $\rho(T)$ curves of the 19 nm sample for 0, 1, 3, and 5 T fields with the MR(T) curves in the magnetic field of the 5 T.

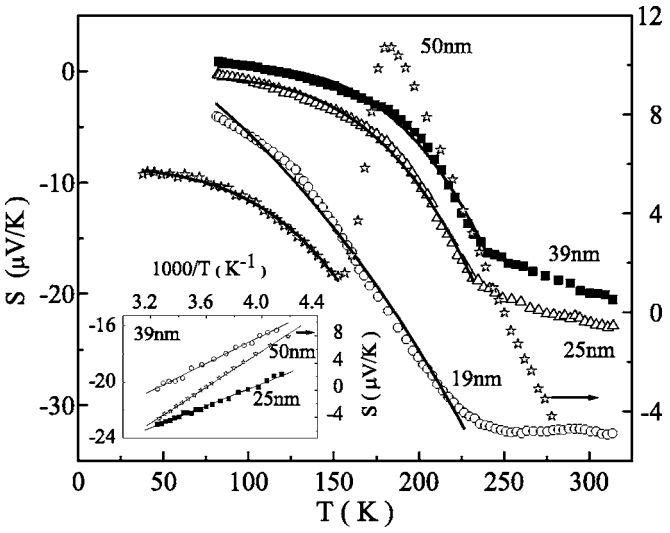

FIG. 8. Thermal variation of thermopower as a function of T with $S(T)$ vs $1000/T$ curves in the inset.

D. Thermopower

The thermal variation of thermopower $S(T)$ of all the samples is shown in Fig. 8. For the 19 and 25 nm samples, S is negative throughout the temperature range studied, but for the 39 nm sample S is positive in the interval of 77 and 114 K, while for $T>114$ K, S changes its sign. The transition to the FM state is marked by a steep rise of S towards zero. The nature of $S(T)$ for the 50 nm sample is quite different from that of the other three samples of lower dimensions. For the 50 nm sample, with the decrease of the temperature from 280 K, $S(T)$ increases slowly and attains a maximum value at around 217.5 K close to the metal-insulator transition point. Then $S(T)$ decreases sharply with the fall of temperature and finally shows a broadened hump with further decrease of temperature. S remains positive from 77 to 280 K, but above 280 K the thermopower attains a negative value. The sharp increase of S in the vicinity of T_C is a manifestation of the sudden change of spin entropy due to the enhancement of the spin polarization caused by the magnetic transition. Above the peak of the $S(T)$ curve the thermal variation of S follows the adiabatic small polaron hopping theory,[37] obeying the following relation:

$$S(T) = (k_B/e)(\alpha + E_S/k_BT), \tag{8}$$

where E_S is the activation energy for the TEP and α is a sample dependent constant. Above 218 K the linearity of S vs $1000/T$ curves implies the validity of the adiabatic small polaron hopping theory for S. The activation energy of the 50 nm sample obtained from the linear fitting of the S vs $1000/T$ curve (inset of Fig. 8) is 13.3 meV, whereas the activation energy obtained from conductivity is found to be 154.2 meV. The large discrepancy between the activation energies for conductivity E_ρ and thermopower E_S is a hallmark of polaronic transport. Table III contains the E_S values of the samples studied. Similar to the phonon drag effect, the carrier-magnon interaction gives rise to a magnon drag effect which can be expressed as $S_m=(C_m/ne)\alpha_n$, where n is the carrier density corresponding to the contribution of the magnon specific heat C_m and $\alpha_n<1.0$. Since the magnon specific heat of the ferromagnets varies as $T^{3/2}$ we can expect a $T^{3/2}$ contribution in TEP for the ultrafine Sr-doped $NdMnO_3$ particles studied here. Below the MI transition the $S(T)$ curves in the ferromagnetic metallic region are found to obey a relation[38] such as

$$S(T) = S_0 + S_{3/2}T^{3/2} + S_4T^4, \tag{9}$$

where the extrapolation of the high temperature $S(T)$ vs $1000/T$ curve offers the value of S_0 (Fig. 8). The second term presents the spin wave contribution, but the origin of the third term is not known. The coincidence of the experimental and the fitted curves upholds the importance of the role of the spin wave carrier interaction in the ferromagnetic metallic region of $S(T)$.

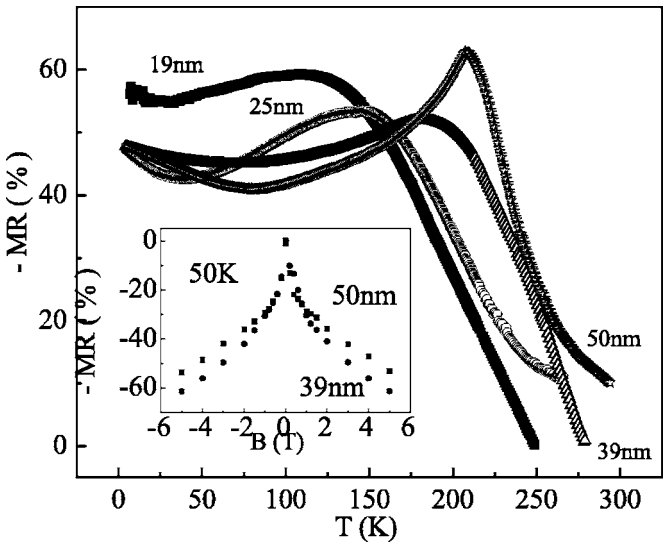

FIG. 7. Magnetoresistance of the four samples as a function of temperature for 5 T field. Inset presents the field dependence of MR(T) of the 39 and 50 nm samples as a function of H at 50 K.

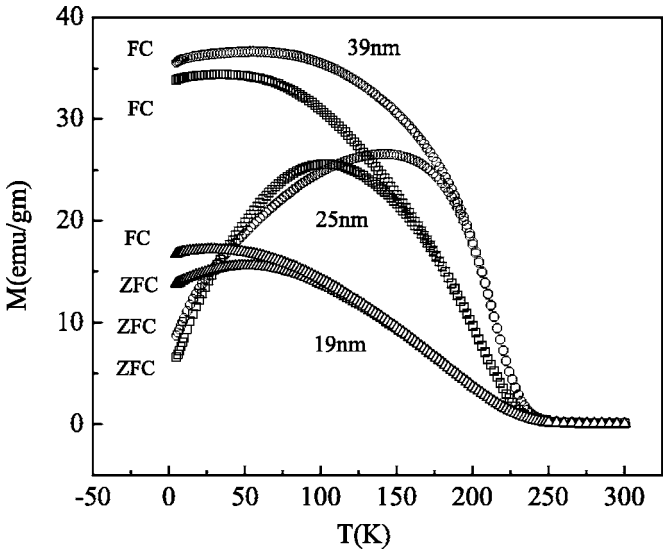

FIG. 9. Field cooled and zero field cooled dc magnetizations of the 19, 25, and 39 nm samples as a function of temperature under a magnetic field of 200 Oe.

E. Magnetic measurement

Figure 9 shows the temperature dependence of the field cooled (FC) and zero field cooled (ZFC) magnetization $M(T)$ measured as a function of temperature while warming the sample from 5 K under a field of 200 Oe. The magnetization in the ZFC mode exhibits a broadened paramagnetic to ferromagnetic transition at T_C due to the ferromagnetic spin ordering in the Mn sublattice with a peak at T_B. T_C is determined from the inflection point of the field cooled $M(T)$ curve as observed in the dM/dT vs T curve. T_C values increase with an increase in particle size. In the temperature range of 250–300 K the data follow a Curie-Weiss law $\chi = C/(T-\Theta)$, where C is the Curie-Weiss constant and Θ is the Curie-Weiss temperature. Table II summarizes the variation of the parameters with the particle size. From Fig. 9 it is evident that due to the reduction of particle size the long range order suffers severe degradation along with a suppression of the magnetization and the broadening of the PM-FM transition. The transition width increases with the decrease of the size of the particles possibly due to the insufficient annealing of the samples. Among the four samples the maximum magnetization is obtained for the samples with the largest particle size. For fine particle perovskite manganites a decrease in magnetization and an increase in resistivity occur as we decrease the particle size. These magnetic properties of the nanoparticles can be explained invoking the core-shell structure of nanoparticles as discussed in Sec. III B. The core behaves as the the bulk material, whereas the shell may be considered as a disordered magnetic system whose magnetization may be considered to be zero in absence of the magnetic field. As the particle size decreases the shell thickness increases and the volume of the core of the grain decreases thereby reducing the anisotropy of the grain. Again the increase of the shell thickness with the decrease of the particle size enhances the intercore separation between two neighboring grains, resulting in a decrease of the magnetic exchange energy. This explains the decrease of the saturation magnetization with the decrease of the particle size. The thermal energy plays an important role. For lower size grains over a certain range of temperature below T_C the predominance of the thermal energy over the magnetic exchange energy and anisotropy energy hinders the attainment of magnetic ordering though intracore magnetic ordering takes place. For large size grains thermal fluctuation is smaller than the intergrain exchange energy and anisotropy energy and the magnetic ordering can be achieved just below T_C. The wide difference between T_C and T_{MI} originates from the surface strain induced grain boundary effects.[13] In nanoparticles antiferromagnetic insulating regions appear near the grain boundaries, and this region cannot modify the magnetic transition temperature governed by the ferromagnetism of the core, but the insulating nature of the grain boundaries can shift the electrical (MI) transition towards low temperature. The broad ferromagnetic transition may appear from the distribution of the exchange coupling strength originating from the weak magnetic interaction in the vicinity of the grain boundary, the strong intragrain contribution, and also due to the particle size distribution. The broadness of the transition increases with the decrease of the particle size. FC curves which are higher than the ZFC curve but considerably reduced in magnitude show a "Brillouin-like" temperature dependence of the magnetization with a slight downward bending at low temperature. Therefore a large magnetic irreversibility with a very pronounced difference between FC and ZFC curves is observed for the above samples at temperature T_{irr}. These features of the dc magnetization such as the large splitting of the ZFC and FC magnetization curves and the cusp in the ZFC magnetization are signatures of a conventional spin glass.[39] The long range magnetic cluster formation, superparamagnetism, or single domain behavior may also result in wide irreversibility.[3,39]

For a fixed applied field, T_B is found to increase with the increase of the size of the ultrafine particles. This phenomenon can be explained considering the distribution of particle sizes. For a system of magnetic particles with finite volume, T_B varies proportionally with volume V. Therefore the enhancement of particle sizes increases the value of T_B, and the distribution of particle sizes gives rise to a distribution of T_B. In Fig. 10 we have presented the zero field cooled magnetization for the 39 nm sample measured as a function of temperature under a different applied field. The inset of the figure shows the peak temperature T_B of the zero-field cooled $M(T)$ curves as a function of H. T_B decreases as the field increases and is found to obey the following relation:[10] $T_B = a\ln(H)+b$. The fitting with the above relation yields $a = 482.0$ and $b = -55.8$. The origin of this unconventional magnetic field dependence is not known.

Isothermal dc magnetization loops of the nanoparticles were measured at various temperatures (25–250 K), and the loops display ferromagnetic behavior with clear hysteresis. The loops for the samples are more pronounced at the lowest temperature where the magnetization does not saturate. Figure 11 shows the temperature dependence of the remanence for the 25 nm sample. The remanence decreases with the increase of temperature and becomes zero above 250 K. The temperature variation of coercivity H_C of the same sample is

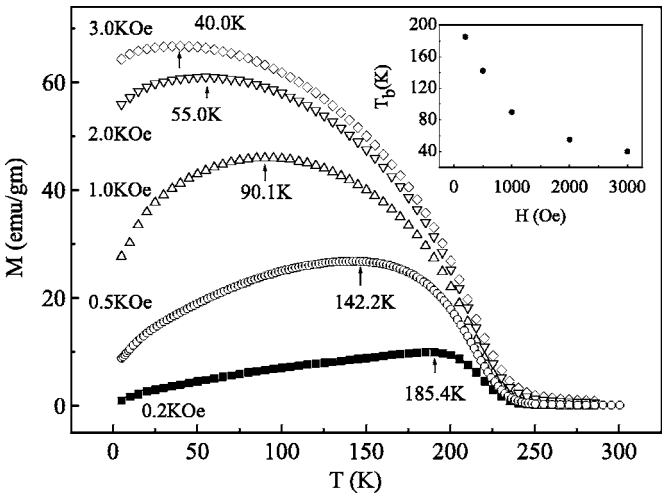

FIG. 10. The temperature dependence of the magnetization under different magnetic fields in the ZFC mode. The inset shows T_B as a function of the magnetic field.

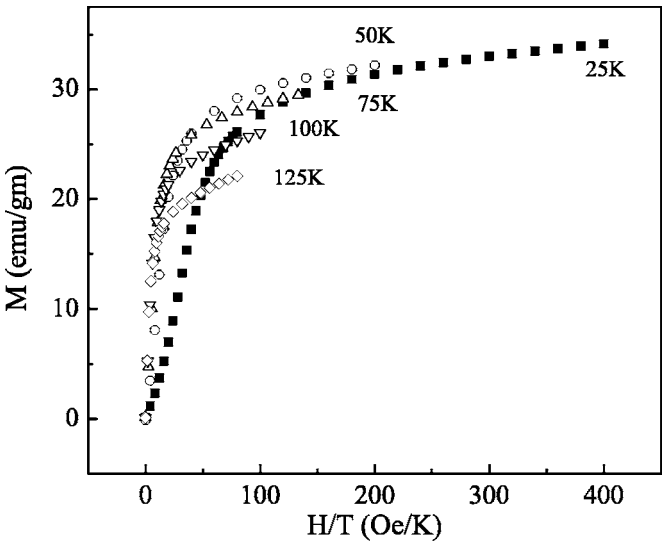

FIG. 12. Magnetization of $Nd_{0.7}Sr_{0.3}MnO_3$ particles with 19 nm size plotted as a function of H/T for 25, 50, 75, 100, and 125 K.

presented in the inset of Fig. 11, and H_C decreases with increase of temperature. The superparamagnetic system follows a relation[40] written as

$$H_C = (2K/M_s)[1 - (T/T_B)^{1/2}], \tag{10}$$

where M_S is the saturation magnetization, K the anisotropy constant, and T_B is the blocking temperature. From the fitting of the H_C vs T curve with the above relation we found the constants $2K/M_S$=673.0 and T_B=212 K. The blocking temperature determined from $M(T)$ curve does not coincide with the above value. Below 235 K the field variation of the magnetization $M(H)$ of nanoparticles presents ferromagnetic behavior at low magnetic field and bends more with the decrease of temperature without any saturation. The experimental criteria[41] for superparamagnetism are (1) the exhibition of the magnetization curve without any hysteresis and (2) the superposition of the magnetization curves at different temperatures in a plot of M vs H/T. To show the constancy of spontaneous magnetization with temperature we have plotted the magnetization of the 19 nm sample as a function of H/T in Fig. 12. The imperfect H/T superposition as observed in Fig. 12 may arise due to a broad distribution of particle sizes, anisotropy effects, etc. However, the TEM measurement shows that the distribution of particle size is narrow. Therefore the particles are not superparamagnetic.

The temperature dependence of the out of phase component (χ'') of the ZFC ac susceptibility for the 19 nm sample is displayed in Fig. 13 at five different frequencies. The inset of Fig. 13 displays a strong peak in χ' followed by a monotonic decrease as T tends to zero. Near about 250 K, χ' abruptly and rapidly decreases to zero, exhibiting the FM-PM phase transition. The whole curve is not symmetric, and there is an indication of a peak near 80 K close to the point at which the ZFC dc magnetization reaches a maximum. The main peak in $\chi'(T)$ should correspond to T_C, but it

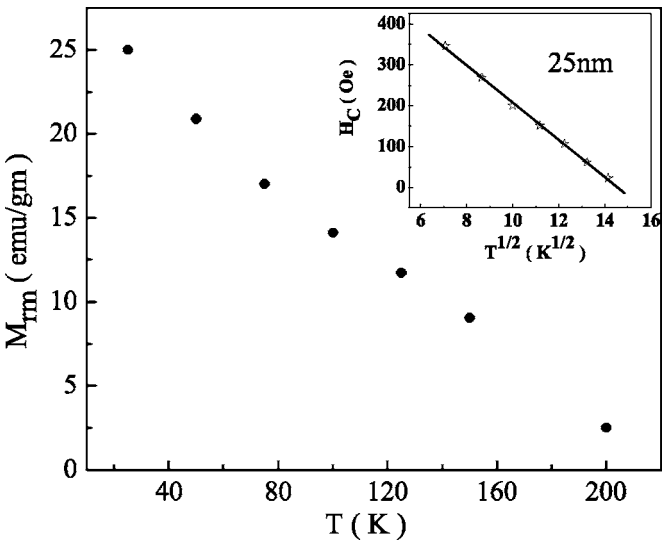

FIG. 11. Remanent magnetization of the 25 nm sample vs temperature. The inset shows coercive field $H_C(T)$ to obey a $T^{1/2}$ dependence.

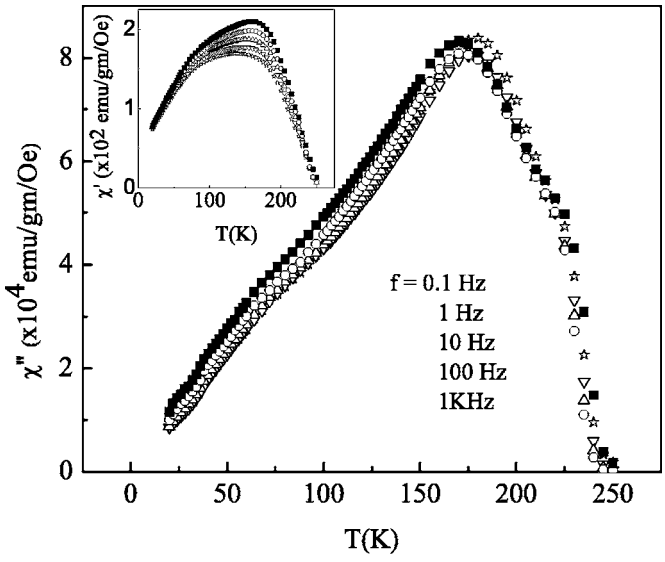

FIG. 13. Temperature dependence of out of phase ac susceptibility (χ'') of the 19 nm sample at 4 Oe ac field for various frequencies. The inset shows the variation of the in-phase ac (χ') susceptibility of the 19 nm sample with temperature for frequencies f=0.1, 1, 10, 100, and 1 KHz.

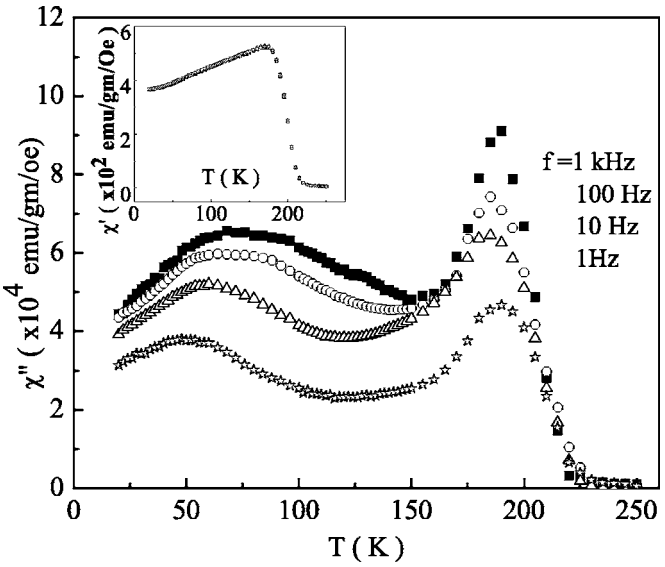

FIG. 14. Imaginary part (χ'') of ac susceptibility measured with 4 Oe ac field for the 50 nm sample for frequencies $f=1$, 10, 100, and 1 KHz. The real part of the ac susceptibility (χ') is displayed in the inset.

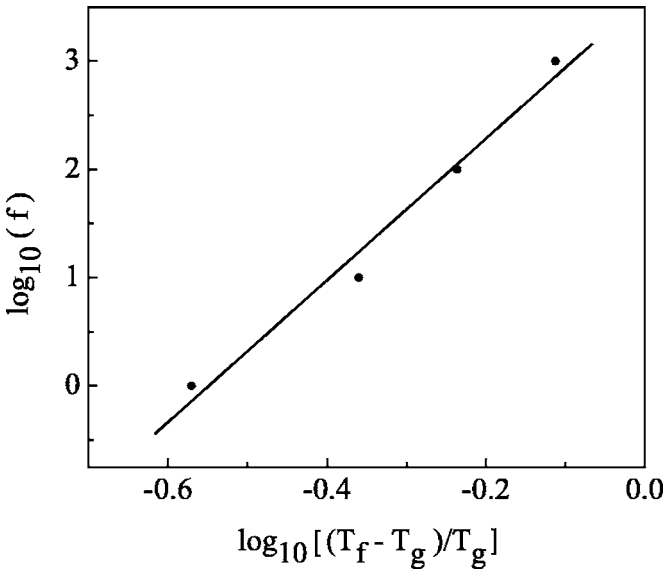

FIG. 15. $\log_{10}(f)$ vs $\log_{10}[(T_f-T_g)/T_g]$ curve with the best fit line.

is worth mentioning that it is more close to T_{irr} in dc magnetization curve. Below the main peak the magnitude of χ' is frequency dependent.

The out of phase component of the ac susceptibility (χ'') provides valuable information on the magnetic energy dissipation or energy loss over a single cycle of an ac magnetic field. In Fig. 14 we observe a sharp peak in $\chi''(T)$ in the vicinity of T_C. The whole curve is not symmetric, but there are indications of a peak close to T_{MI} together with another one near T_B. The magnitude of χ'' is dependent on the frequency. Close examination of $\chi''(T)$, $\chi'(T)$, and dc zero field cooled magnetization reveals that the peak in $\chi''(T)$ is close to T_C. Since $\chi''(T)$ provides the dissipated magnetic energy and maintains a proportionality with the area of the hysteresis loop over one period of the ac field, the peak in $\chi''(T)$ should correspond to the irreversibility temperature T_{irr} where the FC and ZFC magnetizations bifurcate just below T_C. At about 250 K $\chi''(T)$ decreases to zero, exhibiting FM-PM phase transition. The $\chi''(T)$ shows a shoulder near about 235 K and the $d\chi'/dT$ vs T and $d\chi''/dT$ vs T curves reflect a large dip at about 235 K which may be a signature of the breakdown of a large polaron to a smaller one associated with JT lattice distortions.[42] The temperature dependence of the real component (inset of Fig. 14) of the ac susceptibility of the sample with 50 nm size is similar to the dc ZFC magnetization curves, and the nature of the curves are independent of the change of frequency. These curves exhibit a maximum at about 170 K which is frequency independent. The imaginary part of susceptibility $\chi''(T)$ (Fig. 14) shows a sharp maximum at 189 K which is frequency independent. This peak is followed by a broad and frequency dependent cusp at low temperature T_f which increases monotonically with the increasing frequency. The presence of a frequency dependent hump in χ'' is the signature for a cluster glass state.[45] The frequency shift per decade $\Delta T_f/(T_f \log \Delta f)$ is 0.05 which is in good agreement with the typical value for cluster and spin glasses. The appearance of a frequency dependent peak in $\chi''(T)$ well below T_C upholds that the conventional ferromagnetic ordering does not exist here. In order to get an idea about the nature of the low temperature transition, we have plotted T_f values as a function of frequency f (Fig. 15) and estimated the freezing temperature T_g by extrapolating the straight line curve to zero frequency. The frequency dependence can be explained in the light of the critical slowing down of the spin dynamics[39,43,44] written as

$$\tau/\tau_0 \propto [(T_f - T_g)/T_g]^{-z\nu}. \tag{11}$$

Here τ is proportional to f, T_g is the critical glass transition temperature, $z\nu$ is a critical exponent, and τ_0 is the characteristic temperature for the spin dynamics. The fitting with the above relation provides us with the following results: $T_g=41.8$ K, $z\nu=8.07$, and const$\times \tau_0 \approx 10^{-5}$ s. A complete understanding of the magnetic properties of nanomaterials is not simple because of the various factors such as the complexity of nanoparticles arising from the particle size distribution, magnetic interparticle interactions, magnetic anisotropy, surface disorder, etc. Now let us summarize the results of the magnetic measurements to compare with the properties of different magnetic systems. The samples exhibit wide ferromagnetic transition and ZFC-FC irreversibility. Both the irreversibility temperature and the peak temperature of the ZFC curve are magnetic field dependent. The imperfect superposition of M vs H/T curves and the observation of hysteresis at temperatures well above T_B rule out the presence of superparamagnetism in our samples. The particles are single domain in nature. The fact that the coercive field shows a rise as the particle size decreases indicates a multidomain to single domain transition. The frequency dependence of the low temperature peak in χ'' is a reminiscent of a spin glass or cluster glasslike behavior.[45] Both the cluster glass and reentrant spin glass (RSG) exhibits a T_C and a frequency dependent maximum of $\chi''(T)$. The reentrant spin glass and cluster glass have some similarity[46] in the characteristic properties. The RSGs undergo a PM-FM transition at T_C and maintains

a nearly constant value below T_{irr}, whereas the cluster glass shows a finite range ferromagnetic ordering below T_C. But in RSG systems the irreversibility appears at a temperature well below T_C, whereas for a cluster glass the irreversibility arises just below T_C. Considering these characteristic features we can conclude that our samples belong to the class of cluster glass. Moreover, the nonattainment of saturation in the M-H curve is also suggestive of a cluster glass character. The peak temperature in χ' is not frequency dependent, suggesting that the FM state originates from the intracluster ferromagnetism. As the particle size diminishes, the prominence of the characteristic feature of the dynamics of the cluster glass depicted in the frequency dependent peak in χ'' gradually smears out in the main peak.

IV. CONCLUSION

We have prepared $Nd_{0.7}Sr_{0.3}MnO_3$ nanoparticles of different dimensions by the sol-gel process and investigated the effect of the particle size on the structural, transport, and magnetic properties of these ultrafine particles. The Rietveld analysis reveals that Mn–O–Mn bond angles decrease and the bond distance increases with the decrease of the particle size. The resistivity increases with the decrease of the particle size due to the enhancement of the grain boundary effect. The metal-insulator transition temperature T_{MI} decreases with the reduction of the particle size. Both intergrain spin polarized tunneling as well as spin fluctuation are effective to produce the MR in these samples. The intergrain spin polarized tunneling is more effective at low temperature, whereas spin fluctuation is operative near the magnetic transition temperature. The FC and ZFC magnetizations increase with an enhancement in particle size. The ZFC peak temperature T_B and irreversibility temperature T_{irr} are field dependent and decrease with the decrease of the particle dimension. Analysis of dc and ac magnetizations upholds a cluster glasslike behavior for the nanoparticles studied here. The 19, 25, and 39 nm particles are single domain particles but not superparamagnetic, but 50 nm particles show quite different electrical conduction and magnetic behavior, indicating that they fall in the multidomain region.

ACKNOWLEDGMENTS

The authors thank A. K. Pal for technical assistance and Professor B. G. Ghosh for useful discussions. The authors are also grateful to Pulak Roy of the Biophysics Division of SINP and Dr. S. Giri of IACS, Kolkata for providing us the TEM facility.

[1] *Magnetic Properties of Fine Particles*, edited by J. L. Dormann and D. Fiorani (North-Holland, Amsterdam, 1992) .
[2] *Nanostructures and Mesoscopic Systems*, edited by W. P. Kirk and M. A. Reed (Academic, New york, 1992).
[3] D. L. Leslie-Pelecky and R. D. Rieke, Chem. Mater., **8**, 1773 (1996).
[4] R. Skomski, J. Phys.: Condens. Matter **15**, R841 (2003).
[5] R. W. Siegel, Phys. Today **46**(10), 64 (1993).
[6] M. A. Kastner, Phys. Today **46**(1), 24 (1993).
[7] A. P. Alivisatos, Science **271**, 933 (1996).
[8] G. A. Prinz, Science **282**, 1660 (1998).
[9] Ll. Balcells, J. Fontcuberta, B. Martinez, and X. Obrradors, Phys. Rev. B **58**, R14697 (1998).
[10] R.-W. Li, H. Xiong, J.-R. Sun, Q.-A. Li, Z.-H. Wang, J. Zhang, and B.-G. Shen, J. Phys.: Condens. Matter **13**, 141 (2001).
[11] Z.-H. Wang, T.-H. Ji, Y.-Q. Wang, X. Chen, R.-W. Li, J.-W. Cai, J.-R. Sun, and B.-G. Shen, J. Appl. Phys. **87**, 5582 (2000).
[12] T. Zhu, B. G. Shen, J. R. Sun, H. W. Zhao, and W. S. Zhou, Appl. Phys. Lett. **78**, 3863 (2001).
[13] Y. Fu, Appl. Phys. Lett. **77**, 118 (2000).
[14] Y.-H. Huang, C.-H. Yan, Z.-M. Wang, C.-S. Liao, and G.-X. Xu, Solid State Commun. **118**, 541 (2001).
[15] T. Yi *et al.*, J. Phys. Chem. Solids **61**, 1407 (2000).
[16] Z. Q. Jin, H. X. Qin, J. R. Zhang, and Y. W. Du, J. Phys.: Condens. Matter **12**, 3497 (2000).
[17] *Colossal Magnetoresistive Oxides*, edited by Y. Tokura (Gordon and Breach, New York, 2000).
[18] M. B. Salamon and M. Jaime, Rev. Mod. Phys. **73**, 583 (2001).
[19] J. M. D. Coey, M. Viret, and S. von Molnar, Adv. Phys. **48**, 167 (1999).
[20] A. P. Ramirez, J. Phys.: Condens. Matter **9**, 8171 (1997).
[21] A. J. Millis, P. B. Littlewood, and B. I. Shraiman, Phys. Rev. Lett. **74**, 5144 (1995).
[22] M. Imada, A. Fujimori, and Y. Tokura, Rev. Mod. Phys. **70**, 1039 (1998).
[23] G. C. Xiong, Q. Li, H. L. Ju, S. N. Mao, L. Senapati, X. X. Xi, R. L. Greene, and T. Venkatesan, Appl. Phys. Lett. **66**, 1427 (1995).
[24] J. Rodriguez-Carvajal, Proceedings of the Satellite Meeting on Powder Diffraction of the 15th Congress of the IUCR, Toulouse, France, 1990 (unpublished), p. 127.
[25] N. Zhang, W. Ding, W. Zhong, D. Xing, and Y. Du, Phys. Rev. B **56**, 8138 (1997).
[26] P. Dey and T. K. Nath, Phys. Rev. B **73**, 214425 (2006).
[27] P. Sheng, B. Abeles, and Y. Arie, Phys. Rev. Lett. **31**, 44 (1973).
[28] G. J. Snyder, R. Hiskes, S. DiCarolis, M. R. Beasley, and T. H. Geballe, Phys. Rev. B **53**, 14434 (1996).
[29] T. Holstein, Ann. Phys. (N.Y.) **8**, 343 (1959); D. Emin, *Electronic Structure Properties of Amorphous Semiconductors* (Academic, New York, 1973).
[30] G. N. Austin and N. F. Mott, Adv. Phys. **18**, 41 (1969).
[31] N. F. Mott and E. A. Davis, *Electronic Processes in Noncrystalline Materials* (Clarendon, Oxford, 1979).
[32] M. Battabyal and T. K. Dey, J. Phys.: Condens. Matter **18**, 493 (2006).
[33] A. Banerjee, S. Pal, and B. K. Chaudhuri, J. Chem. Phys. **115**, 1550 (2001).
[34] M. Viret, L. Ranno, and J. M. D. Coey, Phys. Rev. B **55**, 8067 (1997).
[35] M. Jaime, M. B. Salamon, M. Rubensteion, R. E. Treece, J. S. Horwitz, and D. B. Chrisey, Phys. Rev. B **54**, 11914 (1996).
[36] H. Y. Hwang, S.-W. Cheong, N. P. Ong, and B. Batlogg, Phys. Rev. Lett. **77**, 2041 (1996).
[37] M. F. Hundley and J. J. Neumeier, Phys. Rev. B **55**, 11511 (1997).
[38] P. Mandal, Phys. Rev. B **61**, 14675 (2000).
[39] J. A. Mydosh, *Spin Glasses: An Experimental Introduction* (Taylor & Francis, London, 1993).
[40] R. C. O'Handley, *Modern Magnetic Materials: Principles and Application* (Wiley, New York, 2000).
[41] C. P. Bean and J. D. Livingston, J. Appl. Phys. **30**, 120S (1959).
[42] D. N. H. Nam, R. Mathieu, P. Norbald, N. V. Khiem, and N. X. Phuc, Phys. Rev. B **62**, 1027 (2000).
[43] K. Gunnarsson, P. Svedlindh, P. Norbald, and L. Lundgren, Phys. Rev. Lett. **61**, 754 (1988).
[44] J. Wu and C. Leighton, Phys. Rev. B **67**, 174408 (2003).
[45] A. Maignan, C. Martin, F. Damay, and B. Raveau, Phys. Rev. B **58**, 2758 (1998).
[46] *Recent Progress in Random Magnets*, edited by D. H. Ryan (World Scientific, London, 1992).